Soft Matter

Nonequilibrium structure formation in electrohydrodynamic emulsions

Journal:	*Soft Matter*
Manuscript ID	SM-ART-08-2023-001110.R1
Article Type:	Paper
Date Submitted by the Author:	04-Nov-2023
Complete List of Authors:	Kach, Jeremy; Carnegie Mellon University, Chemical Engineering Walker, Lynn; Carnegie Mellon University, Department of Chemical Engineering Khair, Aditya; Carnegie Mellon, Chemical Engineering

Soft Matter

ARTICLE TYPE

Cite this: DOI: 00.0000/xxxxxxxxxx

Nonequilibrium structure formation in electrohydrodynamic emulsions[†]

Jeremy I. Kach, Lynn M. Walker, and Aditya S. Khair[*]

Received Date
Accepted Date

DOI: 00.0000/xxxxxxxxxx

Application of an electric field across the interface of two fluids with low, but non-zero conductivities, gives rise to a sustained electrohydrodynamic (EHD) fluid flow. In the presence of neighboring drops, drops interact via the EHD flows of their neighbors, as well as through a dielectrophoretic (DEP) force, a consequence of drops encountering disturbance electric fields around their neighbors. We explore the collective dynamics of emulsions with drops undergoing EHD and DEP interactions. The interplay between EHD and DEP results in a rich set of emergent behaviors. We simulate the collective behavior of large numbers of drops; in two dimensions, where drops are confined to a plane; and three dimensions. In monodisperse emulsions, drops in two dimensions cluster or crystallize depending on the relative strengths of EHD and DEP, and form spaced clusters when EHD and DEP balance. In three dimensions, chain formation observed under DEP alone is suppressed by EHD, and lost entirely when EHD dominates. When a second population of drops are introduced, such that the electrical conductivity, permittivity, or viscosity are different from the first population of drops, the interaction between the drops becomes non-reciprocal, an apparent violation of Newton's Third Law. The breadth of consequences due to these non-reciprocal interactions are vast: we show selected cases in two dimensions, where drops cluster into active dimers, trimers, and larger clusters that continue to translate and rotate over long timescales; and three dimensions, where drops form stratified chains, or combine into a single dynamic sheet.

1 Introduction

Soft matter systems exhibit fascinating collective dynamics as their individual constituents are driven out of equilibrium via an external forcing[1–7]. It is desirable to control such dynamical behavior to enable stimuli-responsive, reconfigurable materials, with potential applications including drug delivery and medicine[8–10]; separations for environmental remediation and material extraction[11–15]; and microrobotics[16]. Active agents, such as particles, drops, or micro-organisms, can move via a number of physico-chemical mechanisms, such self-diffusio- and self-electro-phoresis[17–19], surface-driven flows[20–23], and hydrodynamic locomotion[24,25]. Recent work has focused on active drops that spontaneously move via Marangoni flows[20,21]. These drops exhibit net motion with no external forces applied; rather, the drops move due to interfacial stresses that drag the surrounding fluid. Such motions bear resemblance to those of microscopic living systems, with characteristic interactive behaviors such as predator-prey dynamics. As a result, active droplets are an attractive synthetic model system for studying the collective behavior of living organisms[20], and the development of designer materials[26].

The nonequilibrium motion of active drops requires the consumption of a fuel source, which could be the solubilization of the drop itself in a micellar surfactant solution, or a precursor in a reaction that produces surfactant[20,21]. Observation of the individual and collective behavior of active drop systems can thus be difficult at long timescales, due to finite limitations in the fuel available[27]. Effort has also been made to design systems that undergo collective motion via external energy input, such as with electric and magnetic fields[28–32], light[33], or acoustics[34]. However, using external fields to drive force-free motion of drops, as opposed to rigid particles, has received less attention. It is thus of interest to examine drop-based systems that exhibit emergent collective behavior under an externally applied field, which thereby overcome the limitations of a finite fuel source, in order to predict dynamical structure formation order an extended duration. Here, we introduce electrohydrodynamic (EHD) emulsions as a new system to study collective dynamics in field-driven soft matter, where drop interactions are driven by application of an externally applied electric field. The use of an external electric field would, in principle, overcome the limitation of a finite fuel source that occurs in other active drop systems.

Electrohydrodynamics was first analyzed by Taylor[35,36], who

---

Department of Chemical Engineering, Carnegie Mellon University, Pittsburgh, Pennsylvania 15213, USA
[*] E-mail: akhair@andrew.cmu.edu

[†] Electronic Supplementary Information (ESI) available: See DOI: 10.1039/cXsm00000x/

demonstrated that an electric field applied across the interface of two immiscible fluids with low, but non-zero, electrical conductivities, results in sustained fluid flow. We will refer to the velocity field of this flow as an electrohydrodynamic (EHD) flow. While the EHD flow around a single drop, which induces deformation and potential breakup of the drop, is well understood[37,38], the interactions between drops due to EHD flows has, until recently, received less focus. These interactions are rich because in addition to interaction due to EHD flow, a pair of drops will also interact due to dielectrophoresis (DEP)[39,40]. The latter occurs because of the disturbance of the ambient electric field cause by the presence of the drops. That is, the total interaction between drops is a combination of EHD and DEP[41,42]. Under DEP alone, particles and drops arrange into chain-like structures, where the electrostatic energy of interaction is minimized[43]. This effect is of interest in: (i) electrorheology, where Brownian particles can be toggled between a chained state, with increased resistance to shear, and a homogeneous state[44,45]; and (ii) directed assembly, where arrangement of particles at high concentrations gives rise to a host of accessible crystal structures[46,47]. EHD flow complicates the interactions of drops compared to DEP alone, introducing a hydrodynamic interaction that depends on the electrical and fluid properties of the system, and influencing the pairwise dynamics of drops in tandem with DEP[48]. The hydrodynamic EHD flow results in a longer-range interaction compared to the electrostatic DEP, giving rise to a rich set of distance dependent behaviors for a drop pair. For a pair of identical drops, the interplay between EHD and DEP results in parallel or perpendicular alignment of the pair relative to the field axis (compared to just parallel for DEP only); attraction and repulsion parallel to the field axis (compared to just attraction for DEP only); and a critical separation distance at which EHD and DEP balance and the drop pair ceases to attract or repel. Surfactant at the drop interface weakens the EHD interaction due to an opposing Marangoni flow[49]. When a pair of drops are dissimilar in either electrical conductivity, permittivity, or viscosity, the EHD interaction between them ceases to be “equal and opposite"[50,51], an apparent breaking of Newton’s third law[52,53]. Pairs of dissimilar drops interacting via EHD can exhibit predator-prey interactions, and the emergence of “swimming" drop pairs has been predicted. These non-reciprocal interactions arise due to non-conservative nature of the hydrodynamic interaction due to the EHD flows around each drop. For a pair of dissimilar translating drops, labeled A and B for this example, this manifests as the velocities $\boldsymbol{U}_A \neq -\boldsymbol{U}_B$ (in constrast, for identical drops interacting under EHD and DEP, $\boldsymbol{U}_A = -\boldsymbol{U}_B$) and the center of mass of the pair need not be constant in time. Out of equilibrium, non-reciprocal interactions are have been observed in active droplet systems[54], as well as in broader contexts, such as in neural networks[55] and social dynamics[56]. In EHD emulsions, the emergence of non-reciprocal interactions offer a promising alternative to fuel-limited active drop systems[27], and thus it is of interest to analyze the collective dynamics in EHD emulsions, which is the central goal of the present work. Notably, the works mentioned above focused on the combined EHD and DEP interactions between a pair of drops, with some extension to three and four drops[50]. We present dynamic simulations of large numbers of drops interaction via EHD and DEP, and characterize the collective behavior observed due to the richness of the interactions described above. In section 2, we introduce and describe the interactions between drops due to an externally applied electric field, and walk through the methodology of our simulations. In section 3, we present results for the simulation of emulsions that are monodisperse in material properties in both two and three dimensions, and discuss the effect of material property choices on the bulk structures observed. In section 4, we move to emulsions that are bidisperse in material properties, again in both two and three dimensions, and show the effect of non-reciprocal interactions and how they can be leveraged to observe a variety of collective dynamics. In section 5, we offer some concluding remarks.

2 Dynamical simulation of EHD emulsions

2.1 Field-driven interactions of drops

We consider an emulsion of N spherical drops of radius a_i, electrical conductivity σ_i, permittivity ε_i, and viscosity μ_i, suspended in a surrounding fluid with properties σ_s, ε_s, and μ_s, under action of an external uniform electric field $\boldsymbol{E} = E\hat{\boldsymbol{E}}$, where E is the magnitude of the applied field and $\hat{\boldsymbol{E}}$ is the direction. We allow the possibility that drops can be dissimilar in material properties , such that in some cases $\sigma_i \neq \sigma_j$, $\varepsilon_i \neq \varepsilon_j$, and $\mu_i \neq \mu_j$. In this work, all drops are assumed to be identical in size, such that $a_i = a_j = a$. We assume that the conductivities of the drop and suspending phases are small but nonzero[35,37], and that surface charge convection and relaxation can be neglected. We assume creeping flow, a steady electric field, that the drops maintain a spherical shape, and that drops do not coalesce. Our previous work has shown that predictions for the interaction of two, three, and four drops based on these assumptions are in qualitative agreement with experiments[50]. Via the Melcher-Taylor leaky dielectric model[36], drops with electrical properties distinct from the bulk fluid exhibit a flow tangential at the drop interface with velocity field

$$\boldsymbol{u}_i(r=1,\theta) = \frac{\beta_i}{2}\sin(2\theta)\hat{\boldsymbol{\theta}}. \tag{1}$$

Equation (1) is akin to the surface velocity of the squirmer model for a micro-organism that stirs the surrounding fluid without undergoing locomotion[57], where θ is the polar angle between the position vector and the electric field axis, such that $\theta = \arccos(\hat{\boldsymbol{r}}\cdot\hat{\boldsymbol{E}})$. Equation (1) is dimensionless, with lengths normalized by the drop radius, a, and the velocity normalized by $\varepsilon_s E^2 a/\mu_s$, which arises from balancing the Maxwell and viscous stresses at the drop interface. For a dielectric constant of $\varepsilon_s = 2$, an electric field strength of $E = 1$ kV/cm, a drop size of $a = 1$ mm, and a viscosity of $\mu_s = 0.1$ Pa $\cdot$ s, all reasonable values for an electric field applied across oils, this would give a characteristic velocity of $U = 1.8$ mm/s., which is comparable to that of drops of similar size propelled by Marangoni stresses[20]. These normalizations will be applied throughout the remainder of the paper. The relative strength of the EHD flow produced by any one drop depends on the dimensionless material property ratios $R_i = \sigma_i/\sigma_s$,

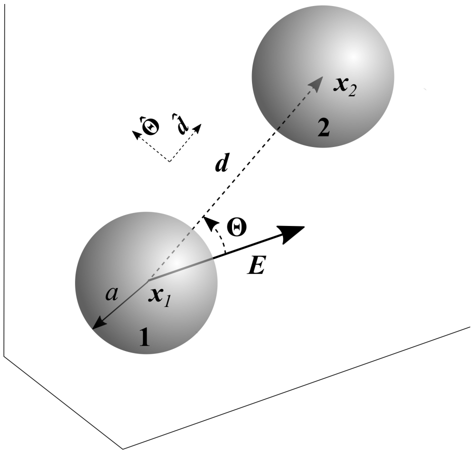

Fig. 1 Schematic of pair of drops. The vector $\boldsymbol{d} = d\hat{\boldsymbol{d}}$ points along the line of centers of the drop pair, and the vector $\boldsymbol{\Theta} = \Theta\hat{\boldsymbol{\Theta}}$ is orthogonal to $\boldsymbol{d}$ and denotes the angle between $\boldsymbol{d}$ and the applied field $\boldsymbol{E}$, such that $\Theta = \arccos \hat{\boldsymbol{E}} \cdot \hat{\boldsymbol{d}}$.

$S_i = \varepsilon_i/\varepsilon_s$, and $M_i = \mu_i/\mu_s$, such that

$$\beta_i = \frac{9}{5}\frac{R_i(1-R_iS_i)}{(1+2R_i)^2(1+M_i)}. \qquad (2)$$

The interfacial velocity described by equation (1) propagates a stresslet flow in the bulk fluid[58,59], the direction of which is determined by the sign of β. Here, $\beta > 0$ describes a flow from the equator to the poles, and $\beta < 0$ describes a flow from the poles to the equator, which are analogous to that of a pusher and puller, respectively, in the squirmer model. A second drop, denoted j, placed in the vicinity of drop i, then translates with the velocity

$$\boldsymbol{U}_j^{EHD}(d,\Theta) = \beta_i \Bigg[\left(\frac{1}{d^2} - \frac{2(1+3M_j)}{2+3M_j}\frac{1}{d^4} \right) P_2(\cos\Theta)\hat{\boldsymbol{d}} - \frac{1+3M_j}{2+3M_j}\frac{1}{d^4}\sin(2\Theta)\hat{\boldsymbol{\Theta}} \Bigg] + O(d^{-5}), \qquad (3)$$

where the superscript U^{EHD} indicates the EHD contribution to the interaction velocity, $P_2(\cos\Theta) = \frac{1}{2}(3\cos^2\Theta - 1)$ is the second Legendre polynomial; $\boldsymbol{d} = \boldsymbol{r}_j - \boldsymbol{r}_i = d\hat{\boldsymbol{d}}$ is the vector connecting the centers of drops i and j; $\Theta = \arccos(\hat{\boldsymbol{d}} \cdot \hat{\boldsymbol{E}})$ is the angle made between $\boldsymbol{d}$ and the applied field direction; and $\hat{\boldsymbol{\Theta}}$ is the direction perpendicular to $\boldsymbol{d}$; as shown in figure 1. A derivation of equation (3) can be found in[48,50]. It can be seen from equation (3) that the interactions between drops i and j are not reciprocal ($\boldsymbol{U}_i \neq -\boldsymbol{U}_j$) when drops i and j have different material properties. The first term in equation (3) acts to repel or attract the drops along the line connecting their centers, and depends both on the separation distance between the drop centroids and the orientation of the pair relative to the electric field direction. This component of the interaction decays the slowest with separation, given the leading order d^{-2} dependence. The second Legendre polynomial in this term changes sign at the critical, or magic, angle $\Theta = 54.7^\circ$, at which orientation the drop pair will neither attract nor repel. The second term acts to reorient the drop pair parallel or perpendicular to the applied field. The reorientation of the drop pair occurs over a shorter range than the attraction/repulsion, as seen by the d^{-4} dependence. The angular dependence of this term has zeros at both $\Theta = 0^\circ$ and $\Theta = 90^\circ$, requiring that the drop pair aligns parallel or perpendicular to the field at long times, depending on the sign of β_i.

In addition to EHD flows, each drop disturbs the ambient electric field around itself, which we assume to be spatially uniform and steady in the absence of the particles. This gives rise to a DEP force acting upon the neighboring drops, and vice versa. The velocity of interaction of a drop j due to its DEP interaction with drop i is[43,48,50]

$$\boldsymbol{U}_j^{DEP}(d,\Theta) = -\frac{12(1+M_j)}{2+3M_j}K_{ij}\frac{1}{d^4}\Big(P_2(\cos\Theta)\hat{\boldsymbol{d}} + \frac{1}{2}\sin(2\Theta)\hat{\boldsymbol{\Theta}} \Big) + O(d^{-5}), \qquad (4)$$

where K_{ij} contains the polarizability of each particle, and is defined as

$$K_{ij} = \frac{1-R_i}{1+2R_i}\frac{1-R_j}{1+2R_j}. \qquad (5)$$

The DEP force acting on a pair of drops is reciprocal, i.e. $\boldsymbol{U}_i = -\boldsymbol{U}_j$ and the center of mass of the drop pair remains stationary (note $K_{ij} = K_{ji}$), as it depends equally on the polarizability of each particle. As shown in equation (4), DEP is a shorter-range interaction (O(d^{-4})) compared to EHD (O(d^{-2})), however the angular dependence for both attraction/repulsion and pair reorientation are similar. In this case, the direction of attraction/repulsion, and alignment parallel or perpendicular to the field direction, depend on the sign of K_{ij}. When K_{ij} is positive, drops tend to align and attract along the field direction, leading to the formation of chains.

The interactions described in equations (3) and (4) together describe the total motion of a drop interacting with its neighbor under a uniform applied electric field, and can be written as

$$\boldsymbol{U}_j(d,\Theta) = \left(\beta_i\frac{1}{d^2} - \Phi_{ij}\frac{1}{d^4} \right) P_2(\cos\Theta)\hat{\boldsymbol{d}} - \frac{\Phi_{ij}}{2}\frac{1}{d^4}\sin(2\Theta)\hat{\boldsymbol{\Theta}} + O(d^{-5}), \qquad (6)$$

where the factor Φ_{ij} contains the combined higher-order effects of EHD and DEP, and is defined as

$$\Phi_{ij} = \frac{2(1+3M_j)}{2+3M_j}\Big(\beta_i + \frac{6(1+M_j)}{1+3M}K_{ij} \Big). \qquad (7)$$

The drop motion described by equation (6) has been discussed in detail for pairs of identical drops[48] and dissimilar drops[50,51].

EHD drives the long-range interaction, while the short-range interaction depends on the combined influence of both EHD and DEP. The relative velocity of a drop pair, $\boldsymbol{U}_j - \boldsymbol{U}_i$, depends closely on the relative position of the drops, while the orientation of the pair at long times, i.e. whether the pair aligns parallel or perpendicular to the field direction, is governed by Φ_{ij}, which depends purely on the material properties of the drops and suspending phase, as shown in equation (7). Experiments in[50] demonstrated that equation (6) accurately predicts the interactions of widely separated drops, qualitatively predicts the interactions of drops pairs even at close separations, and pairwise addition of equation (6) qualitatively captures the dynamics of groups of three and four drops.

2.2 Simulation of N drops

The three-dimensional interactions of many drops under a uniform, steady applied field are simulated using HOOMD-Blue[60]. We study the dynamics of a dilute emulsion of $N = 1000$ spherical drops at an area fraction of $\phi_A \approx 0.05$ when simulating interactions in two dimensions, and a volume fraction of $\phi \approx 0.005$ when in three dimensions. All computations are performed in three dimensions, with two-dimensional motions of drops simulated by confining drops to the plane perpendicular to the applied field, thereby resulting in drop translations only occurring within the confining plane. Drops are contained within a square box with dimension $L = 250$, or a cubic box with dimension $L = 96$. Periodic boundary conditions are employed. Drop motions are governed by the overdamped equation of motion

$$\frac{\mathrm{d}\boldsymbol{x}_j}{\mathrm{d}t} = \boldsymbol{U}_j + \sum_{i \neq j} \frac{1}{\gamma_j} \nabla \phi_{ij}, \;\; j = 1,2,...N, \tag{8}$$

where ϕ_{ij} is an arbitrary interaction potential between drops, and $\gamma_j = (1+M_j)/(2(2+3M_j))$ is the Stokes drag coefficient for a drop. The velocity of each drop is determined as the sum of all pairwise interactions with the neighboring drops

$$\boldsymbol{U}_j = \sum_{i \neq j}^{N} \boldsymbol{U}_{ij}(d_{ij}, \Theta_{ij}). \tag{9}$$

The coordinates d_{ij} and Θ_{ij} are determined using the minimum image convention. By employing the minimum image convention, we are limiting this study to finite systems of drops, unlike fully periodic simulations with methods such as Ewald summation[61]. This, however, is a reasonable treatment in our case due to the low volume fraction studied and our focus on short-range structure formation[62,63]. Given the $O(d^{-5})$ error of equation (6), which is of the same order as the leading three-body interactions[59], determination of the drop motions via pairwise addition is a reasonable assumption for dilute systems.

Drop positions are computed by numerically integrating equation (8) with a forward Euler scheme. Time is scaled by $\tau = \mu_s/\varepsilon_s E^2$, and the timestep used is $\Delta t = 0.005\tau$. Drops are prevented from overlapping via the interaction potential

$$\phi_{ij} = \frac{\gamma_j}{4\Delta t}(2-d_{ij})^2 H(2-d_{ij}), \tag{10}$$

where $H(x)$ is the Heaviside step function. This is effectively an implementation of the potential-free Heyes-Melrose algorithm[64,65], wherein overlapping drops are equally moved to exact contact. Due to the deterministic and anisotropic nature of the interactions, the initial position has a non-negligible influence on later states of the simulation. To mitigate the influence of a given initial state on the observed emulsion behavior, we simulate five different initial states for each set of material properties, and any quantitative metrics shown are taken from averages of the five runs.

3 Monodisperse emulsions

We first simulate the effect of EHD flow on structure formation in monodisperse suspensions of drops. Here, all interactions are reciprocal, such that the center of mass of a pair does not move in the absence of other drops. The way in which EHD flow affects the dynamics of the emulsion can occur via several mechanisms. The direction and strength of the EHD flow depends on the parameter $\beta \propto 1 - RS$. The limit $\beta \to 0$ corresponds to purely DEP interactions, where chain formation occurs. When $\beta > 0$ (< 0), the EHD flow acts to orient drops parallel (perpendicular) to the field axis and repel (attract) in the field direction. Therefore, the EHD flow will always compete with chain formation from DEP in one way or another: repelling drops parallel to field axis but aligning them, or attracting them in the field direction while aligning them in the plane normal to the field. This indicates that both the relative signs and magnitudes of β and Φ control emulsion dynamics. We discuss first the effect of EHD flow on the interactions of drops confined to the plane perpendicular to the applied field axis, and then move to monodisperse emulsions in three dimensions.

3.1 Two-dimensional interactions of drops perpendicular to the field

The confinement of drops to a plane perpendicular to the appied field axis removes a degree of freedom from equation (6); in this case, the dependence of the interaction velocity on Θ. When the field axis is perpendicular to the line connecting the centroids of the drops ($\Theta = 90^\circ$), the interactions between drops become isotropic, and equation (6) is reduced to

$$\boldsymbol{U}_j(d) = -\frac{1}{2}\left(\beta_i \frac{1}{d^2} - \Phi_{ij}\frac{1}{d^4}\right)\hat{\boldsymbol{d}} + O(d^{-5}). \tag{11}$$

Now, drops repel (attract) in the far-field when $\beta < 0$ $(\beta > 0)$, and repel (attract) in the near-field when $\Phi > 0$ $(\Phi < 0)$. Intuitively, when attractive interactions dominate at all separation distances, drops will coarsen into clusters, shown in figure 2b. It is expected that the clusters observed in figure 2b will, at long timescales, coalesce into a single cluster, however coarsening beyond $\tau = 5000$ was not investigated due to long simulation times. In this case, $R = 1$ and $S = 0.1$, such that only the EHD interaction is active, and DEP is not. Inversely, when repulsive interactions dominate at all separation distances, drops will repel and maximize their separations, shown in figure 2c, forming crystal-like configurations where the inter-particle spacing depends on the relative size of the drops and the simulation box, here for EHD interactions where $R = 1$ and $S = 10$. When both EHD and DEP are active, the distance dependent interplay between the two effects will result in structure formation that lies between the two cases shown above. Here, we show an interesting case where the interactions in the plane perpendicular to the field are attractive at long-range and repulsive at short-range, resulting in a stable equilibrium sep-

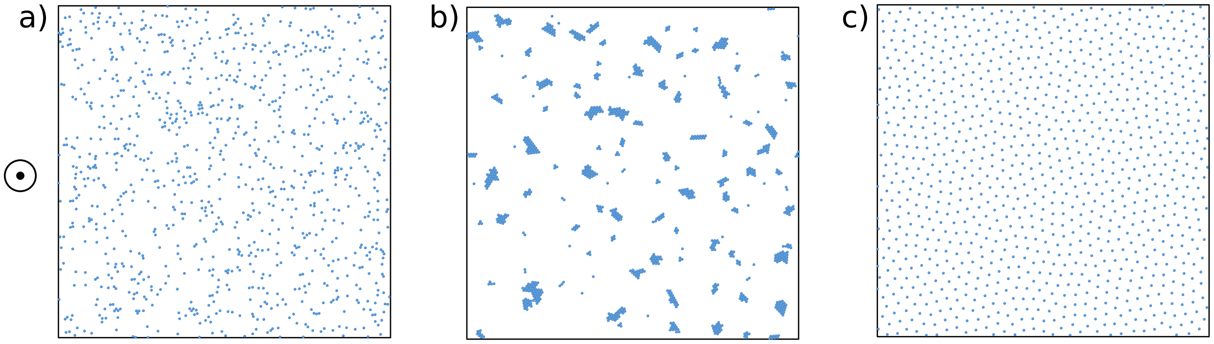

Fig. 2 Simulations of monodisperse EHD emulsion drops confined to the plane perpendicular to the field axis. a) The initial state ($\tau = 0$) of the simulations shown in b) and c). b) Snapshot at final timestep $\tau = 5000$ for drops with $R = 1$, $S = 0.1$, $M = 1$. c) Snapshot at final timestep $\tau = 5000$ for drops with $R = 1$, $S = 10$, $M = 1$.

aration distance of drop pairs that is larger than the separation required for contact but much smaller than the size of the box. This equilibrium position is the separation distance where the leading order EHD flow is balanced by the higher order flow and DEP force, i.e. the critical separation distance,

$$d_c = \sqrt{\frac{\Phi_{ij}+\Phi_{ji}}{\beta_i+\beta_j}}, \tag{12}$$

which can be derived by solving for the separation distance at which the relative velocity $\boldsymbol{U}_i + \boldsymbol{U}_j = 0$[48]. In figure 3 we show a simulation of drops with $R = 0.1$, $S = 1$, and $M = 1$, having started at the same initial position shown in figure 2a. These material properties result in a critical separation distance of $d_c \approx 7$. In figure 3a, which is the final frame of the simulation ($\tau = 5000$), drops are observed to form static clusters, where the drops in clusters are not in contact, yet are at a stable separation from neighboring drops. We can compare the critical separation of a pair of drops ($d_c \approx 7$) to the average separation distance between drops in clusters, determined by the pair correlation function

$$g(r) = V\frac{N-1}{N}\langle\delta(r)\rangle, \tag{13}$$

where V is the volume or area of the box, depending on the dimension, N is the total number of particles, and $\langle\delta(r)\rangle$ is a delta function indicating the presence of drops at a distance r from the center of a neighboring drop, averaged over all drops. Here, we discretize this delta function into bins of 50. Shown in figure 3b, a peak is observed near $r \approx 6$, which is smaller than the predicted critical separation distance for a pair of drops in the absence of any other drops. The decrease in stable separation of drops here can be explained by the influence of the $N-2$ drops surrounding the pair, which exert a long-range attractive interaction at separations of $d_c > 7$. Therefore, while the distance that EHD and DEP balance is approximately 7 for a pair, the added long-range attraction increases the weight of EHD interactions on the balance between effects, effectively reducing the stable drop separation for large numbers of drops. As shown, EHD interactions between drops can give rise to interesting structure formation, tunable by material property choice, when drops are confined to a plane, suggesting that a rich set of collective behaviors for monodisperse systems in three dimensions is possible.

3.2 Drops in three dimensions

In three dimensions, the interactions of drops are substantially more complex. When only DEP interactions are present, drops are known to form chains parallel to the applied field axis[66]. Here, $\Phi > 0$, such that drop pairs orient to align parallel to the field direction ($\Theta = 0$), and attract each other at orientations of $\Theta < 54.7^\circ$ and repel when $\Theta > 54.7^\circ$. This chain formation is a phenomenon of interest in electro- and magnetorheology, as well as directed assembly, where imposition of a external field across a suspension polarizes drops and gives rise to oriented structures[44,67]. Given that DEP interactions are purely electrostatic, a minimum energy configuration exists for a collection of spheres in a uniform applied field, similar to magnetically polarizable particles[47]. However, the microstructural arrangement of drops into chains is considered a kinetic process, due to the short-range interactions and the existence of kinetically arrested states over long processing times[68]. Introducing longer-range, and non-conservative, EHD interactions is expected to impact the kinetics of chain formation and growth, and the addition of hydrodynamic interactions means a minimum energy configuration is no longer available. An example of this for relatively weak EHD flow compared to DEP ($\beta < \Phi$) is shown in figure 4. Figures 4a-c (Videos S1, S2, S3, ESI†) show side views of three-dimensional snapshots at the last time step of the simulations ($\tau \approx 7\times10^5\Delta t$). The relative strength of the EHD flow is tuned between cases by varying the parameter S, with $R = 0.2$ and $M = 1$ held constant. In figure 4a, $S = 4.9$, $\beta = 0.001$, and $\Phi = 0.87$, and drops interact purely by DEP with negligible influence of EHD. Chain formation is observed, as expected. When $S = 0.1$, $\beta = 0.05$ and $\Phi = 0.95$, and the EHD flow acts to align yet repel drops along the field direction. This motion acts to oppose DEP, especially at large separation distances where the $O(d^{-2})$ EHD flow dominates the $O(d^{-4})$ DEP, resulting in the slowing of chain formation. This is exemplified in figure 4b, where the presence of chains is less visible, and drop positions appear more or less still random at late simulation times. The effect is reversed, however, at $S = 16$. Here, $\beta = -0.11$ and $\Phi = 0.69$, and the EHD flow is both opposite that of the previous case and stronger. The long-range EHD flow then

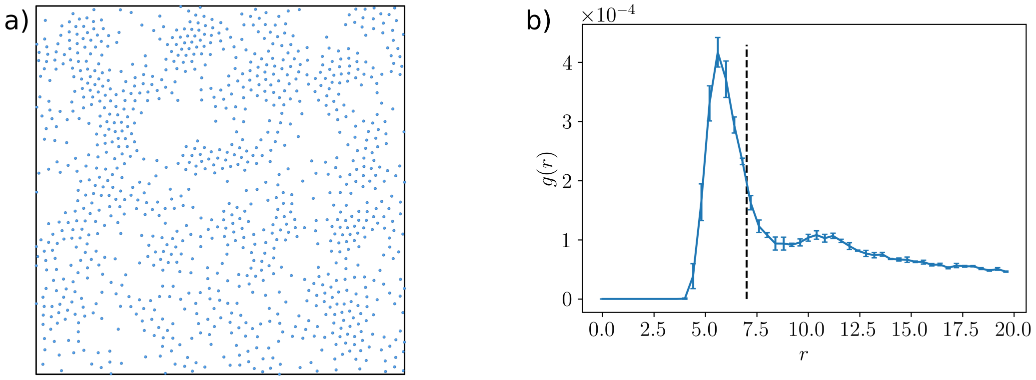

Fig. 3 Simulation for $R = 0.1$, $S = 1$, $M = 1$ for drops confined to a plane, with the applied electric field pointing out of the page and normal to the plane where the drops reside. a) Snapshot of the simulation at the final timestep $\tau = 5000$. b) Radial distribution function $g(r)$ averaged over five simulations at the final timestep $\tau = 5000$. Error bars indicate standard deviation of $g(r)$ at each bin. A large peak is observed at $r \approx 6$, and a softer peak observed at $r \approx 11$. Vertical dotted line corresponds to $d_c \approx 7$ for a pair of drops.

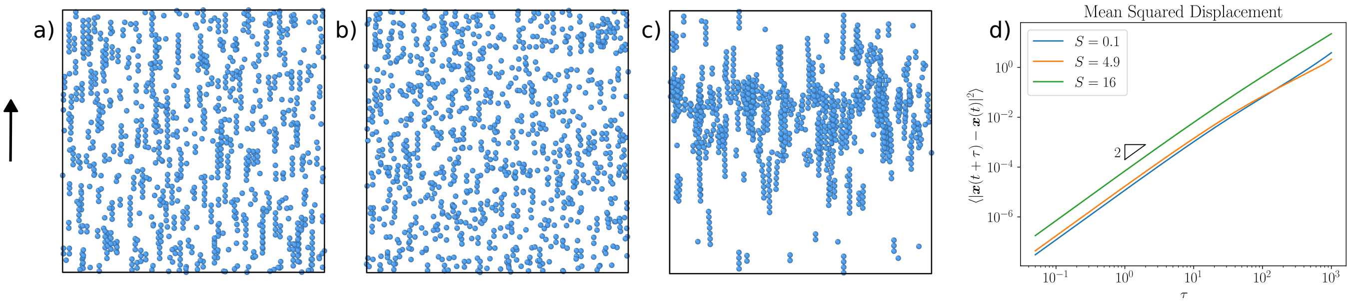

Fig. 4 Simulations for $R = 0.2$ and $M = 1$ with varying S. a) Snapshot of chains at τ_{final} for DEP alone when $S = 4.9$ (Video S1, ESI†). b) Snapshot of chains at τ_{final} for combined DEP and EHD when $S = 0.1$ (Video S2, ESI†). c) Snapshot of chains at τ_{final} for combined DEP and EHD when $S = 16$ (Video S3, ESI†). d) Mean squared displacement of drops at early times in a), b), and c). In all cases drops are shown to undergo ballistic motion, demonstrated by the square exponent of the displacement for each set of material properties.

acts to pull in far away drops along the field axis, where they then align by the shorter-range orientation effect of Φ. This results in longer chains on average, and increased depletion of drops not involved in chaining compared to DEP alone, shown in figure 4c. The effect of the EHD flow on the motion of the drops is shown in figure 4d using the mean squared displacement (MSD). The MSD is calculated as[69]

$$\langle|\boldsymbol{x}(t+\tau)-\boldsymbol{x}(t)|^2\rangle = \frac{1}{N}\sum_{i=1}^{N}\frac{1}{N_{\Delta t}-m}\sum_{k=0}^{N_{\Delta t}-m-1}(\boldsymbol{x}_i(k+m)-\boldsymbol{x}_i(k))^2, \quad (14)$$

where $N_{\Delta t}$ is the number of time steps. We limit evaluation of the MSD to the first quarter of the simulation, i.e. $\tau \leq 1250$, in the above three cases, where we assume drops move steadily toward forming chains yet meaningful chain growth and depletion of chain-forming drops has not started. Here, the motion of drops undergoing chain formation and growth is expected to be a ballistic process[70]. In cases a) $S = 0.1$ and b) $S = 4.9$, the displacements are similar, yet the collective dynamics of the drops are markedly different. It is likely then that while short-range chain formation is mitigated by the competition between EHD and DEP for $S = 0.1$, the increased long-range presence of the EHD flow induces more motion of drops far away, making up for the slowdown in local displacement. The impact of a strengthened EHD flow on the displacement of drops is more prominent for c) $S = 16$. The motion of drops in all cases as they approach chain formation is ballistic, indicated by the square exponent in displacement; however, when $S = 16$ the long-range EHD interaction has a larger influence on drops more widely separated, increasing the total motion of the drops and therefore their net mobility, shown by the upward shift in figure 4d.

Further increasing S results in an increase in the strength of the EHD flow. This corresponds to an increase in $|\beta|$ with $\beta < 0$. While this gives rise to an increase in attractive interactions in the field direction, fewer chains are observed as S increases. An example of this is shown in figure 5. Interestingly, the drops collapse along the field direction into a wavy, sheet-like structure that persists in time, shown in figure 5a (Video S4, ESI†) and b. The location on the vertical axis of the wave-sheet vary with the initial state, however the existence of the sheet occurs in all cases. The structural characteristics of the wave-sheet here bear resemblance to the banding observed in electrokinetic suspensions of particles in AC fields[71], where particles in the bands dynamically rearrange without changing the structure of the bands, and there are visible kinks in the bands with angles of inclination between $50-70°$. We indicate the magic angle of $\Theta = 54.7°$ in figure 5 for

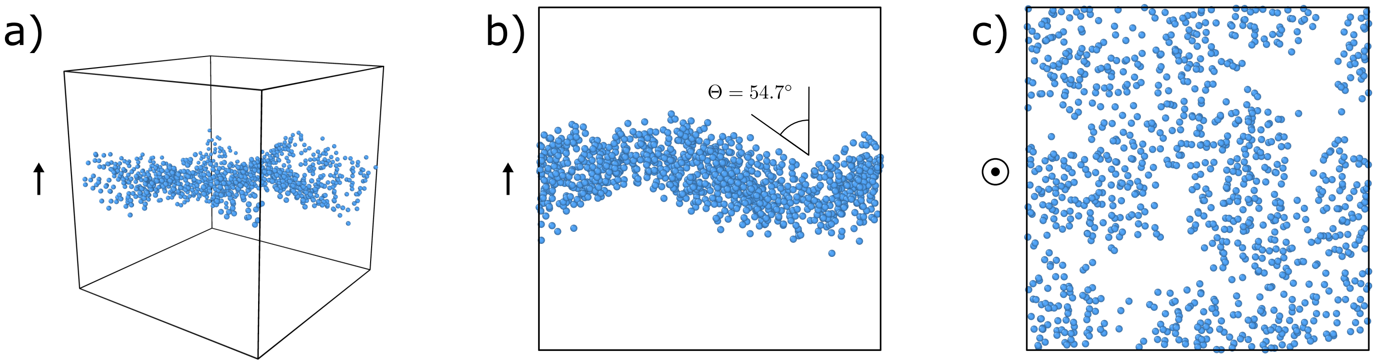

Fig. 5 Simulation for $R = 0.2$, $S = 150$, $M = 1$. a) Three-dimensional view of τ_{final}, where drops are configured into a single, wavy, sheet-like structure (Video S4, ESI†). b) Side view of τ_{final}, with the electric field pointing in the vertical direction. Here one of the coordinate axes planes parallel to the field is shown, however drop interactions are symmetric in the plane perpendicular to the field, such that similar structure is observed upon rotation of snapshot about the field-axis. c) Top view of τ_{final}, with the electric field pointing out of the page. Dynamic clusters are observed, with drops moving within zones of higher density, yet with the macroscopic density distribution holding constant in time.

comparison. Within the wave-sheet, two "phases" coexist, with regions of high and low local drop density, respectively. Drops are not confined to these zones, however, with the drops constantly moving throughout the course of the simulation. At short times, decreasing β results in quickened chain formation, with eventual collapse of the chains into the structures shown in figure 5. However, as β further decreases, chain formation is eventually skipped entirely, and wave-sheet formation occurs immediately. The effect of the interplay between EHD and DEP on chain formation is determined more clearly by comparing the fraction of drops that are in chain-like configurations with at least one other drop, shown in figure 6. Drops are considered part of a chain if they are in contact with another drop ($d \leq 2.05$), and the pair is oriented in the field direction ($\hat{\boldsymbol{d}} \cdot \hat{\boldsymbol{E}} \geq 0.95$). The fraction of drops in chains at a given timestep are then averaged over five initial states for the same material properties. This gives a clear sense of how quickly drops join chains and the stability of chains over time. The cases shown in figure 4, of a) $S = 0.1$, b) $S = 4.9$, and c) $S = 16$, all exhibit monotonic growth in the populations of chained drops, with the slight exception of $S = 16$, where the fraction of chained drops plateaus and fluctuates about a maximum value of around 0.6. These results match the intuition from discussing figure 4, where the addition of an EHD flow that repels neighboring drops in the field direction inhibits chaining, compared to DEP alone when $S = 4.9$. This further evidences the long-range effect of the EHD flow, given the decrease in chain formation kinetics, yet comparable overall displacements between $S = 0.1$ and $S = 4.9$ observed in figure 4d. For $S = 16$, when EHD is strengthened, but now with an attractive flow in the field direction, drops quickly arrange in chains compared to DEP alone. In this case, initial chain formation is relatively fast, and then levels off as chains no longer take in new drops, but move relative to each other. This behavior hints toward the collapse of drops into the wave-sheets observed at higher S and more negative β. As seen in figure 6a, when $S = 38$ ($\beta = -0.34$), initial arrangement of drops into chains is fast, until chains are destroyed and drops collapse into the wave-sheet structures observed in figure 5. It is notable here that the leading order EHD flow is in the same direction as DEP, however EHD and DEP compete to orient drop pairs relative to the field direction, which is quantified by equation (7). Via equation (5), the DEP contribution to Φ is always positive for identical drops, while β can change sign and decreases linearly with increasing S. Thus, as β decreases, the overall attraction of drops in the field direction strengthens, yet the orientational change of the drop pair continues to decrease, given that Φ is linear in S. We expect this to contribute to the nonmonotonic chaining observed for moderate values of S, where the initial chaining is due to local alignment of drops to their nearest neighbors, at an increased rate due to the EHD flow. However, as chains continue to form, the strong attraction in the field direction continues to pull drops together, causing the chains to coalesce and collapse onto each other. Thus, the monodisperse emulsions exemplify two effects: i) that EHD flow, for $\beta < 0$, drives drops into wave-sheet structures due to long-range attraction in the field direction; and ii) that the interplay between EHD and DEP, given by the sign and magnitude of Φ, determines whether accelerated chain formation occurs, even at increasingly negative β, before structural collapse. We parameterize this interplay by comparing the relative magnitudes of β and Φ as

$$\Gamma = \frac{|\beta| - |\Phi|}{|\beta| + |\Phi|}, \tag{15}$$

plotted against S in figure 6b. Chain formation that appears stable over long times occurs when $|\beta| \ll |\Phi|$, which corresponds to the limit of $\Gamma \to -1$. Note that $\beta > 0$ is constrained by the numerator $1 - RS$, and scales similarly with R as K in equation (5). Therefore, for positive β, $|\beta| \ll \Phi$ always, and EHD will inhibit chain formation but never fully overcome it. As β becomes more negative, we see an increased rate of chain formation, with clear qualitative differences in the chain-like structures observed, and collapse of the chains toward a plane normal to the field axis. The case of $S = 38$ corresponds to $|\beta| \approx |\Phi|$, corresponding to $\Gamma \approx 0$, with $\beta < 0$ and $\Phi > 0$, where now the collapse of chains towards a common plane also results in the destruction of chains and formation of a wave-sheet structure. This continues to occur as $\Phi \to 0$ and $\Gamma \to 1$,

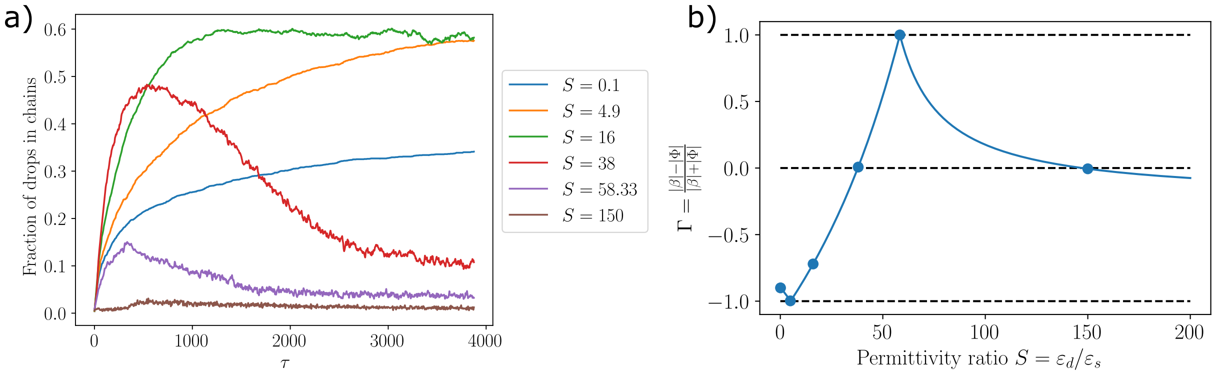

Fig. 6 Effect of EHD versus DEP interactions on the proclivity for drops to form chains. a) Fraction of drops in chains versus simulation time, with each curve corresponding to the number of drops in chains at each time step, averaged across five runs with varying initial states. b) Comparison of the leading order radial EHD flow strength (given by β) to the rotational interaction strength (a combination of EHD and DEP given by Φ) as a function of in the permittivity ratio, S.

albeit with drastically reduced chain formation to start with. As β decreases further, drop pairs avoid alignment with the field direction entirely when $\Phi < 0$ and $\Gamma \approx 0$, the interactions of which are analogous to those described by Park & Saintillan[72] for particles interacting via a combination of induced-charge electroosmosis (ICEO) and DEP. Note that Φ varies linearly with β, and thus large values of $|\beta|$ require $\Gamma \to 0$. They also do not observe chain formation, as ICEO acts in a similar manner as EHD flow when $\beta \ll 0$, however instead of a dynamic wave-sheet structure, their simulations show more homogeneous chaotic motion of particles in three dimensions. We attribute this discrepancy to their use of a fully periodic Ewald summation of particle interactions versus our minimum image convention, which is again supported by the formation of dynamic band structures similar to the wave-sheet we observe in monolayer experiments in a finite domain of particles interacting under ICEO[71]. The effect of R, S, and M on Γ is shown in a phase map in figure 7. Figure 7 shows that the behaviors described by figure 6 occur for a variety of values of R and S for equiviscous drops, meaning that variable chain formation and wave-sheet observation is possible for more material property ratios than just those considered in the present work.

It is clear from the results above that for monodisperse emulsions, the material properties of drops and the suspending fluid are levers with which to tune the nonequilibrium structures of EHD emulsions. Specifically, by varying the relative permittivities (S) and conductivities (R), the chaining commonly observed in field driven suspensions can be either inhibited, enhanced, or destroyed entirely.

4 Bidisperse emulsions

Recent work has demonstrated that two dissimilar drops may undergo non-reciprocal EHD interactions[27], via theoretical calculations[50] and boundary integral simulations[51]. While pairwise DEP interactions are always reciprocal, since the polarization of each drop contributes equally to the relative motion of the pair, hydrodynamic interactions due to the EHD flow depend only on the properties of the drop instigating the flow. As a result, the center of mass of the drop pair can move in time, and the pair can undergo tandem locomotion in certain cases, i.e. here it is as if the pair "swims" as a single entity. The dynamics of bidisperse EHD emulsions now cannot be described by a single set of two parameters β and Φ. We use "bidisperse" here to refer to dispersity in the material properties of the drops, a convention we employ for the remainder of the text. Instead, the interactions are governed by six distinct property specific parameters β_i, β_j, Φ_{ii}, Φ_{jj}, Φ_{ij}, and Φ_{ji}, given by equations (2) and (7). A couple of cases in two and three dimensions are examined to exemplify the impact of non-reciprocal interactions on the dynamics and structure of EHD emulsions.

4.1 Two-dimensional interactions of drops perpendicular to the field

Given the complexity of non-reciprocal interactions between drops just discussed, a simpler view of the effect of nonreciprocity can be explored with only isotropic interactions in two dimensions. Here, interactions are purely attractive or repulsive, in similar fashion to simulations of chemiphoretic interactions of particles, of which pairs can have variable mobilities (attractive/repulsive) depending on their relative properties[62,63]. The crucial difference here is that the distance-dependent interplay between EHD and DEP is expected to factor into the bulk behavior of the emulsions. The direction and strength of these attractive and repulsive interactions are determined by the combination of the six β and Φ parameters mentioned at the beginning of the section. Due to the material property dependence of β and Φ, not all combinations of attraction and repulsion are possible. A tiling of some expected simple cases is shown in figure 8. It is worth noting that figure 8 does not represent the full phase map of all types of non-reciprocal interactions, due to the fact that the distance dependence of EHD versus DEP gives rise to a large set of unexpected behaviors that are difficult to predict *a priori*. We can develop an intuition, however, for how more complicated dynamics will manifest by discussing the simplest cases, shown in figure 8. In figure 8a, the interactions between A-type drops, B-type drops, and A-B drops are all attractive. Here, the net inter-

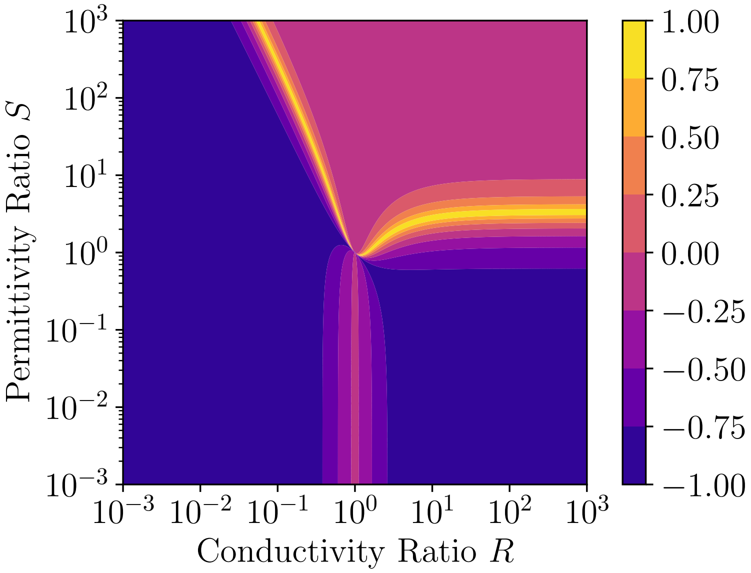

Fig. 7 Map of Γ for all values of R and S, with $M = 1$. Colors correspond to the magnitude of Γ, with bright yellow when $\Gamma = 1$ and dark blue when $\Gamma = -1$.

action between A and B drops is attractive, but it is possible that the EHD flow from A drops may push away B drops, but B drops pull in A drops more strongly, for instance. The intuition, regardless, is that composite clusters are formed consisting of both types of drops. The opposite case is shown in the figure 8b. Here, the net interactions between all species are repulsive, and drops are expected to repel neighbors into nearly regularly spaced crystal structures. When A drops repel, B drops attract, and A and B drops repel, phase separation is expected, shown in figure 8c. This occurs when $\beta_A > 0$, $\beta_B < 0$, and $\Phi_{AB} + \Phi_{BA} > 0$. An alternate case, where both A's and B's cluster without mixing is not possible, since this would require the following conflicting conditions: (i) the EHD flows of both A and B drops are both attractive ($\beta_A, \beta_B < 0$), and stronger than DEP interactions ($\Phi_{AA}, \Phi_{BB} < 0$), and (ii) the DEP interactions of the dissimilar pair are repulsive and stronger than the EHD interactions $\Phi_{AB} + \Phi_{BA} > |\beta_A + \beta_B| > 0$, of which both cannot be simultaneously satisfied. The last case presented is when both A and B drops repel drops of their own type, yet A-B interactions are net attractive, shown in figure 8d. This is the case shown in figure 10b & c of[50], and figure 3 of[51]. Here, drops are expected to pair with drops of the opposite type while repelling drops of their own type, resulting in dimer "swimmers". Beyond two drops, we will show more exotic structure can emerge, including stationary trimers where drops of one type are equally spaced around drops of the opposite type.

The first case we present involves drop interactions that follow the bottom left of figure 8. To achieve this, we use the material properties $R_A = R_B = 1$, $S_A = 10$, $S_B = 0.1$, $M_A = M_B = 1$. The condition $R = 1$ results in turning off any DEP interactions. This corresponds to the interaction parameters $\beta_A = -0.9$ (repulsive when $\Theta = \pi/2$), $\beta_B = 0.09$ (attractive), $\Phi_{AA} = \Phi_{AB} = \frac{8}{5}\beta_A$, and $\Phi_{BA} = \Phi_{BB} = \frac{8}{5}\beta_2$. From the parameters alone, it is expected that A drops will repel themselves, B drops will attract themselves, and A-B pairs will repel due to the stronger repulsion of A winning out. This is shown in figure 9. The final frame of the simulation is shown in figure 9a (Video S5, ESI†). A drops, shown in blue, repel into a semi-regular pattern, while B drops, shown in red, form small clusters in the interstices between A drops. The repulsive EHD flow instigated by the A (blue) drops is an order of magnitude larger than the attractive flow from the B (red) drops ($\beta_1/\beta_2 = 10$), which results in the formation of clusters of B drops that are then broken up by repulsive interactions with neighboring A drops. This effect is shown in figure 9b, which shows the largest cluster size over time, averaged between five simulations with varying initial conditions. At first, the B (red) drops are dispersed, and cluster formation only occurs at the pairwise level. After the A (blue) drops spread out to steady separation distances, B drop clusters grow as the B drops travel through the isotropic repulsive field around the A drops. Eventually, the B drops connect and form larger clusters, however those clusters become too large compared to the spacing between the A drops, and are then broken up due to the repulsive flow from the A drops. The separation distance between the A drops decreases when surrounding a cluster of B drops. Here, the attractive flow of the B drops draws in the surrounding A drops. Evidence of this is found by computing $g(r)$ for only the A drops, shown in figure 9c. The two peaks indicate the spacing between A drops surrounding a cluster of B drops (first peak), and the larger spacing between A drops when there are no attractive B drops in the vicinity (second peak). A suggested set of materials that may recover the above described behavior is castor oil and water drops suspended in silicone oil. The results here suggest that phase behavior can be tuned by drop material properties to achieve desired structures; e.g. a composite can be made of evenly spaced dissimilar drops (repulsive and comparable β_A and β_B), small clusters of one type surrounded by the other (the present case), or even a single large cluster of one type surrounded by a dispersion of the other (large, attractive β_A versus smaller, repulsive β_B).

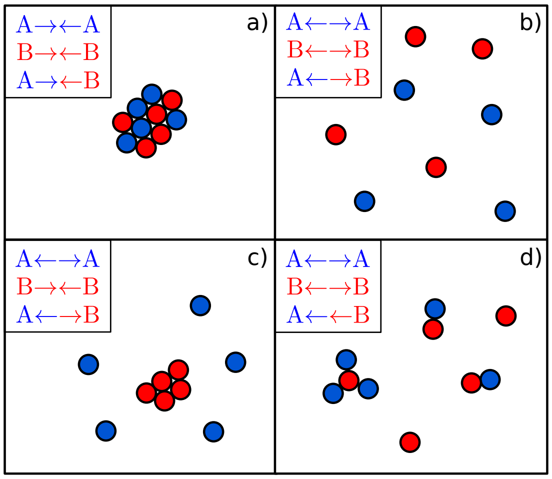

Fig. 8 Subset of non-reciprocal phase behaviors predicted by equation (6). Each quadrant corresponds to a different set of the directions of interactions between types of drops. The letters and arrows in the corner of each quadrant represent the direction of the interactions for *AA* pairs, *BB* pairs, and *AB* pairs.

We have just shown that structures in the plane perpendicular to the field axis can be designed and modified via choice of material properties. Next, we show that a new set of material properties, albeit in the same planar format, can give rise instead to dynamic structures with distinct, motile "agents." This is shown in figure 10 (Video S5, ESI†). Here, $R_A = 10$, $R_B = 0.1$, $S_A = S_B = 1$, and $M_A = M_B = 1$, corresponding to $\beta_A = -0.18$, $\beta_B = 0.056$, $\Phi_{AA} = 0.59$, $\Phi_{BB} = 2.79$, $\Phi_{AB} = -1.83$, and $\Phi_{BA} = -1.45$. The A (blue) drops repel themselves by EHD flow at long-range, and through a dominant DEP at short-range. The B (red) drops attract at long-range through EHD and strongly repel at short-range through DEP; this is the same case as figure 3. The non-reciprocal A-B interaction is net repulsive at long-range ($\beta_A + \beta_B < 0$), yet strongly attractive at short-range ($|\Phi_{AB} + \Phi_{BA}| \gg \beta_A + \beta_B$), giving an unstable equilibrium point where EHD and DEP balance[51]. The combination of these interactions results in a variety of qualitative behaviors. The evolution from the initial state to dynamic structure formation is shown in figure 10a & b, with 10a a view of the initial state and 10b a snapshot at $\tau = 2500$, or halfway through the simulation. The inset of figure 10b gives a glimpse of the variety of structures formed, with selected structures indicated with dashed circles. At short-range, B drops attract A drops more strongly than A drops attract B drops. This results in a depletion of A drops into clusters with B drops, which have a larger composition of A compared to B, leaving unclustered B drops remaining. This leaves small, spaced-out clusters of B drops, which mimic the behavior of monodisperse drops of the same material properties, shown in figure 3. Looking at the composite clusters containing both A and B drops, dimer "swimmers" and n-mer "snakes" develop and evolve, and then move in the direction of the B drop head-group, which again are pulling A drops more strongly than the A drops pull back. Trimers form obtuse triangles with a B drop at the corner with the large angle, and "swim" along the axis of symmetry. A quadramer can be seen in the middle of the inset, where three A drops are evenly spaced around a B drops, thus preserving symmetry and therefore not translating. Below the quadramer and cluster of B drops in the middle, a 5-mer is observed, which has rotational symmetry but no mirror symmetry, and rotates like a "rotor". Finally, in the bottom right corner of the inset, a kinked, snake-like structure is observed. This cluster undergoes no net motion, but acts as a "flapper", with the three drops on each side of the central B drop undulating back and forth such that the central B drop periodically translates about some nearly steady position. Compared to the previous example, shown in figure 9, the combination of non-reciprocal EHD interactions and the distance dependent interplay between EHD flow and DEP force give rise to a zoo of collective behaviors. An analogy is readily made to active matter systems, where symmetry breaking results in emergent collective behaviors[54,73]. However, unlike most active systems, the dynamics here are driven by an external field as opposed to the consumption of a fuel source (e.g. depleting solute while moving up a concentration gradient, or co-solubilization between drops), which offers the ability to experimentally study the collective dynamics predicted here at very long timescales. We analyze the motion of two types of clusters in the "zoo," namely a "swimming" dimer and rotating quintamer in figure 11. The motion of the clusters is captured through trajectory maps and calculation of the velocity autocorrelation of a drop within the cluster, with the velocity autocorrelation defined as $\langle \boldsymbol{U}(t+\tau) \cdot \boldsymbol{U}(t) \rangle$. The trajectory of the "swimming" dimer is captured through the trajectory of the blue A drop propelling the dimer, shown in the inset of figure 11a. Motion of the dimer is analyzed over $\sim 30000\tau$ (about 3/5 of the simulation time), the range of time between formation of the dimer and collision of the dimer with another cluster to form a larger cluster. The dimer is observed to undergo linear directed motion over large distances during this time period, with slight direction changes occurring due to interactions with neighboring clusters. The speed of the dimer remains nearly constant throughout its existence, since the directed motion of the cluster is a result of the asymmetric interactions between a connected pair of an A and B type drop, which are at their strongest when the drops are in contact. This is re-

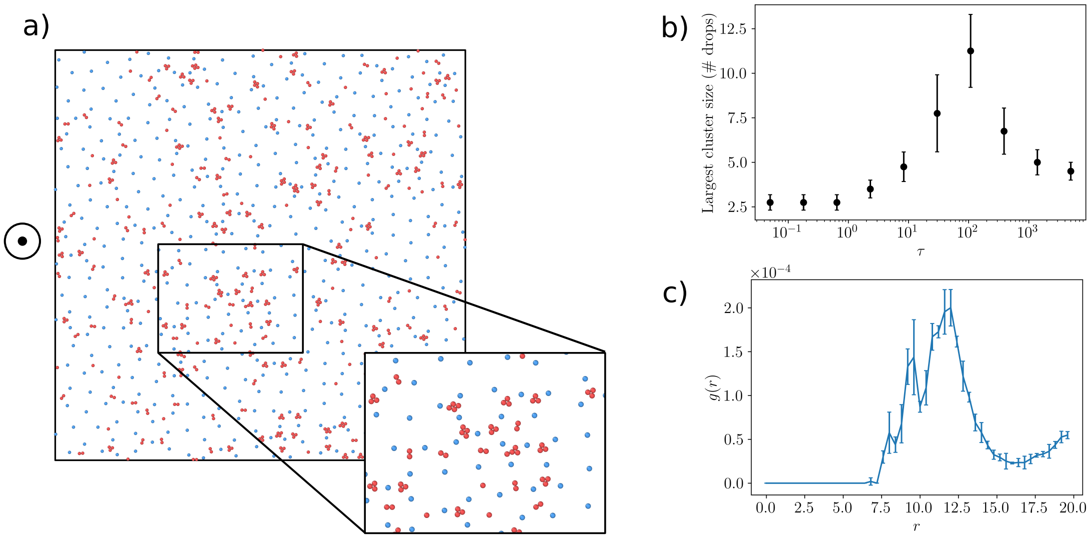

Fig. 9 Simulation for $R = 1$, $S_A = 10$, $S_B = 0.1$, $M = 1$ of drops confined to the plane normal to the applied field (Video S5, ESI†). The field is pointing out of the page. a) Snapshot at τ_{final}, with the A drops shown in blue and the B drops shown in red. The inset shows a zoomed-in look at a subset of the drops in the plane. b) Largest cluster size of red B drops over time, averaged between five runs with varying initial states. Error bars represent standard deviation between runs. c) Average of radial distribution function $g(r)$ over five runs for blue A drops at τ_{final}. Error bars represent standard deviation between runs.

flected in the velocity autocorrelation, shown in figure 11b, where the velocity of the dimer persists over $4000 - 5000\tau$, where after the pair continues to move at nearly constant speed but ultimately ends up translating in the opposite direction, demonstrated by a $C_v \approx -1$ at the largest timescales. Motion of the rotating quintamer is also analyzed over a time period of $\sim 30000\tau$, where now the motion of two drops are tracked to capture the full dynamics of the cluster. Figure 11c shows the trajectories of both an A-type drop on the outside of the cluster (solid line) and the A drop at the center of the cluster (dotted line). From the trajectory map, it is clear that the "rotor" is rotating in a nearly consistent fashion, while the cluster as a whole translates due to the net interactions of the surrounding drops and clusters. The dynamics of the rotation is captured in figure 11d, where the velocity autocorrelation of the outside drop (solid line) is shown to oscillate at a nearly constant period of $\sim 2000\tau$, consistent with the drop rotating at a constant rate about the center of the cluster. In addition to rotating, the cluster, as mentioned, translates through the domain, shown by the trajectory of the center drop (dotted line) in figure 11c and the velocity autocorrelation of the center drop (dotted line) in figure 11d. The velocity of the center drop persists over a longer timescale, similar to that of the "swimming" dimer shown in figure 11b. One such set of materials that could result in the above described behaviors is castor oil and fluorinated oil drops suspended in silicone oil, where castor oil and fluorinated oils would have conductivities larger and smaller than silicone oils, respectively, while having permittivities at a similar order to silicone oils. Notably, we only consider steady fields, and it is possible that even more rich behaviors could be observed when the field is scheduled in time.

4.2 Interactions in three dimensions

As shown in the previous section, a wide variety of qualitative behaviors are observable with non-reciprocal, isotropic EHD interactions. In three dimensions, the orientation of the drops relative to the field axis adds another layer to the already complex non-reciprocal interactions observed in two dimensions. In this section, we explore the same material property combinations simulated in the previous section, but now allow the drops to move in all three dimensions. Having characterized the range of possible structural behaviors for monodisperse emulsions, we now seek to apply that intuition to bidisperse emulsions.

The first case we discuss is for populations of drops between which have equal conductivities and differing permittivities. Specifically, we consider the instance where $R_A = R_B = 1$, $S_A = 10$, $S_B = 0.1$, and $M_A = M_B = 1$. Here, as with the same system in two dimensions, the fact that $R = 1$ results in no DEP interaction between drops; EHD only are operative. In three dimensions, the A drops form wavy sheets, similar to those observed in figure 5. The B drops orient along the field axis, yet repel, and therefore remain homogeneously dispersed over time. When the two populations of drops are combined in equal proportion, all drops become incorporated into a single wave-sheet, shown in figure 12. Figures 12a & b show the monodisperse behavior of each of the drop types, where $S = 10$ in figure 12a and $S = 0.1$ in figure 12b. Here, as a reminder, $\beta_A = -0.9$ and $\beta_B = 0.09$. The A (blue) drops clearly control the non-reciprocal interaction, a consequence of $|\beta_A| \gg |\beta_B|$. B (red) drops, which on their own repel in the field direction, are instead drawn into the wave-sheet formed by the A drops. With no DEP interaction, the interaction between drops is purely hydrodynamic, and therefore the total interaction is simply the superposition of monodisperse EHD interactions. The formation of a single wave-sheet, even when half

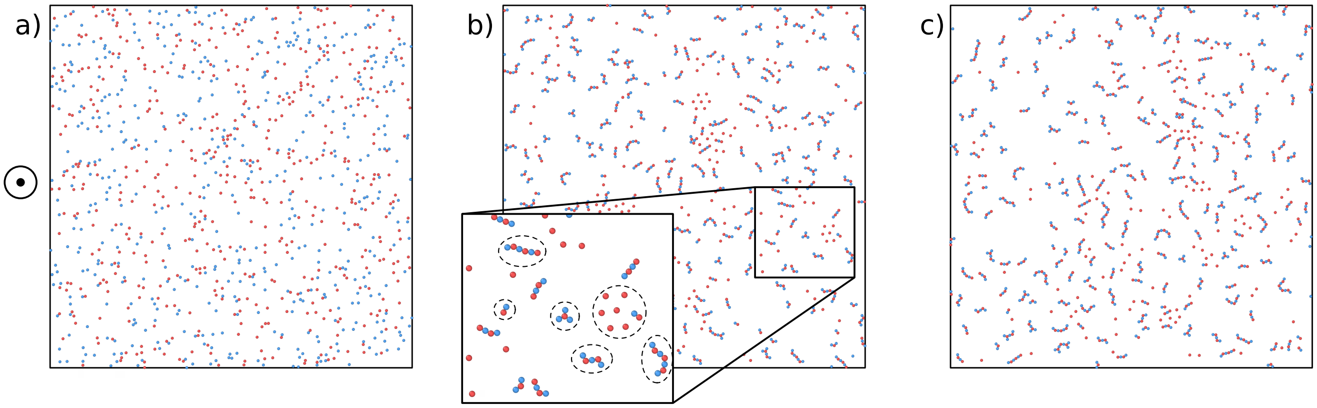

Fig. 10 Simulation for $R_1 = 10,\ R_2 = 0.1,\ S = 1,\ M = 1$ of drops in the plane perpendicular to the applied field axis (Video S6, ESI†). Field points out of the page. a) Initial state of one of the simulations. b) Snapshot of $\tau_{1/2} = 2500$. Inset shows a zoomed in portion of the snapshot. c) Snapshot of $\tau_{final} = 5000$.

of the drops do not form such structures on their own, shows that the stronger EHD flow will dominate the interactions. It is expected, then, that a bidisperse suspension of EHD drops and passive tracers will exhibit the same behavior as that expected for the EHD drops alone, albeit with slower dynamics on the route to steady structure formation. This is exemplified in figure 12d. In order to quantify the rate of sheet formation, the standard deviation of the z−position of all 1000 drops is computed, then averaged over the five initial conditions at each time step. The monodisperse emulsion in figure 12a collapes to the wave sheet twice as quickly as the bidisperse emulsion, a clear consequence of the competitive interaction between the A and B drops.

Next we simulate the same system as figure 10, of drops with equal permittivities and disparate conductivities. Again in this case, $R_A = 10$, $R_B = 0.1$, $S = 1$, and $M = 1$. When this system is confined to a plane perpendicular to the field axis, we observed a rich set of behaviors, such as spaced clustering, and the formation of “swimmers", “snakes", “rotors", and other dynamic configurations. It is therefore of interest to observe how the interactions that give rise to those behaviors will affect three-dimensional structure formation and dynamics. Both A- and B-types in this instance form chains parallel to the field axis in monodisperse emulsions, however the balance of the EHD and DEP interactions of the B drops ($R_B = 0.1$) results in a critical separation distance of $d_c = 7$, as discussed in section 3. Here, however, alignment along the field axis is the dominant orientational behavior, and now the critical separation distance becomes an unstable equilibrium point, where drops attract for $d < 7$ and repel for $d > 7$. The A-B interaction was shown to be net attractive perpendicular to the field, and therefore should be repulsive along the field axis. This is observed in the three-dimensional simulations in figure 13a & b, where chains of pure A and B, respectively, are formed, without any inter-mixing of species (Video S7, ESI†). It is expected that the repulsive (for $d > 7$) EHD flow will slow chain formation for the B-type population, and this is shown to have a mild effect on the fraction of chained drops in figure 13. The fraction of A (blue) drops in chains increases more quickly initially than the B drops (red), which follows intuition given that the EHD flow for $R = 10$ acts to move drop pairs in the same direction as the DEP force. However, by the final time point of the simulation, there are roughly an equal number of drops involved in chains between the different types. The acceleration of chain formation and growth for the B drops could occur for a number of reasons. For instance, although chain formation is slowed for the B drops at wide separations due to repulsion above the critical separation, the net alignment and resulting attraction of opposite type drops perpendicular to the field axis results in A drops pulling B drops closer together, giving the B drops an opportunity to attract each other that they would not have had if unassisted. Evidence supporting this hypothesis can be seen in figure 13a & b, where chains of A and B drops that are in contact are observed to be of similar lengths, a qualitative observation made across multiple runs with different initial conditions. This result suggests that chain formation of species that may not form chains, or are slow to form chains, can be accelerated by doping with a second drop phase, which would then encourage chain formation of the desired species.

5 Conclusions

We have shown that field-driven interactions between drops in EHD emulsions give rise to a rich variety of collective behaviors. Long-range interactions between drops are due to a combination of EHD ($O(d^{-2})$) and DEP ($O(d^{-4})$). The structure of monodisperse emulsions is determined to closely depend on the interplay between these two effects, quantified by the factor $\Gamma = \frac{|\beta|-|\Phi|}{|\beta|+|\Phi|}$. In the plane perpendicular to the applied field direction, the distance dependent interplay between EHD and DEP is shown to give rise to dispersed clusters, where drops remain stably separated away from contact, yet do not disperse evenly throughout the medium. In three dimensions, when $\Gamma \to -1$, DEP dominates the interactions between drops, which assemble into chains, as seen in electrorheological suspensions. When $\Gamma \to 1$, EHD dominates the interactions, and drops are observed to condense into wave-sheet configurations, the structure of which are dynamic yet stable over long times.

Simulations of bidisperse systems of drops were also per-

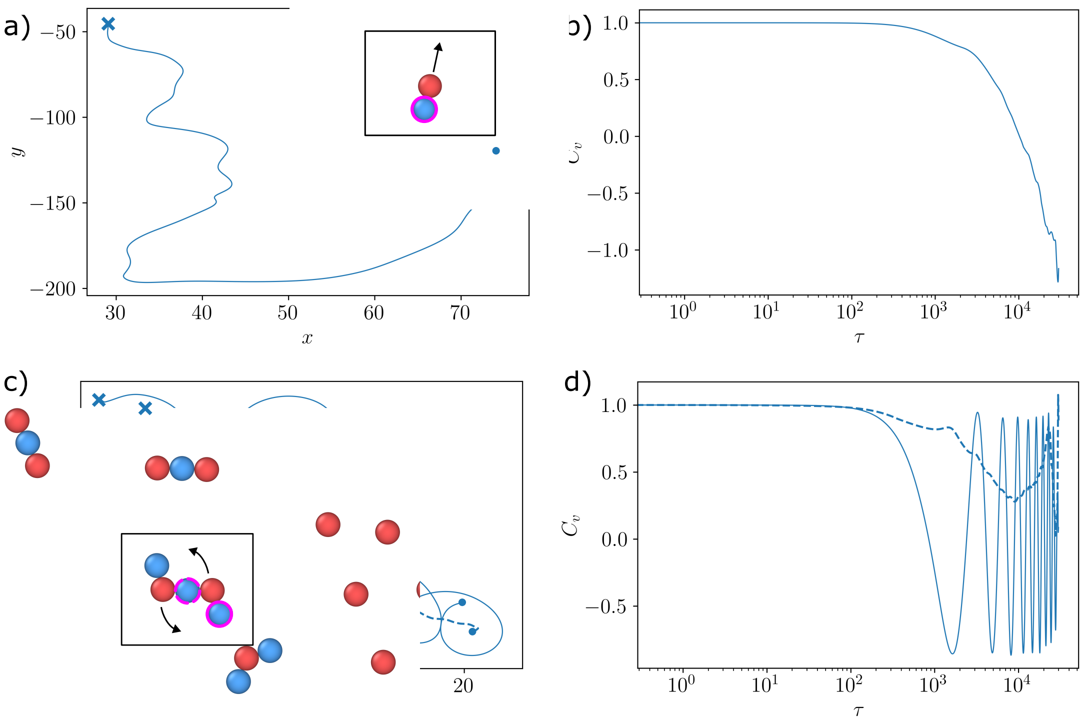

Fig. 11 Analysis of motion of two cluster types observed in the "zoo" of figure 10. a) Trajectory of a blue A-type drop (circled in solid pink in the inset, with the arrows indicating the direction of motion of the entire cluster) in a "swimming" dimer over the course of ~ 70000 time steps (3/4 of the simulation), between when the dimer is formed and when it collides and joins another cluster. The solid circle indicates the initial position of the drop and the cross indicates the final position. b) Velocity autocorrelation of the A drop in the dimer over ~ 70000 time steps. c) Trajectory of two drops in a rotating quintamer over ~ 70000 time steps. The solid line corresponds to the trajectory of the blue A drop (circled in solid pink in the inset) and the dotted line corresponds to the trajectory of the center A drop (circled in dotted pink). d) Velocity autocorrelation of the two A drops indicated in c). The solid line corresponds to the trajectory of the blue A drop (circled in solid pink in the inset, with the arrow indicating the direction of motion of the entire cluster) and the dotted line corresponds to the trajectory of the center A drop (circled in dotted pink). The solid circle indicates the initial position of the drop and the cross indicates the final position.

formed. Results were shown for cases where drops with strong repulsive flows break up small clusters of drops with weaker attractive flows. In a specific case, net attractive interactions between drops of different material properties give rise to a multitude of drop configurations, where "swimmers", "snakes", "rotors", and "flappers" were observed, with a clear analogy to synthetic active matter systems. In three dimensions, two cases were explored. In the first, one drop type was shown to form wave-sheets, while the other formed chains, in the absence of the other type of drop. Here, the non-reciprocal interactions favored the wave-sheet forming drops, and both types of drops were swept into wave-sheet formation. In the other case, one drop type has a stronger proclivity for chain-formation, yet the non-reciprocal interactions between drops were shown to encourage chaining of drops that had weaker interactions.

These results exemplify not only the impact of EHD interactions on the structure formation of emulsions under an applied field, but also the variety of structures and dynamics available when considering this mechanism. These results suggest the opportunity for development of field-driven designer composites, where structure can be controlled by selection of constituent materials. Additionally, the planar simulation results suggest experimental realization of synthetic active-matter analogs without requirement of a consumable fuel source, allowing observation of collective behavior at otherwise inaccessible timescales. Since the systems considered here could be realized using oil drops immersed in an oil suspending fluid, electrochemistry can easily be avoided. The external application of the electric field also implies a wide range of opportunities for control of the emulsion structure via scheduling of the field, in addition to the dependence on material properties discussed previously.

Conflicts of interest

There are no conflicts to declare.

Acknowledgements

J.I.K thanks Dr. Ramalingam Kailasham for helpful discussion on processing particle clustering and displacement. We gratefully acknowledge the National Science Foundation for support through Grant No. CBET-1804548, as well as the H. William and Ruth Hamilton Prengle Fellowship in Chemical Engineering and the John E Swearingen, Carnegie Institute of Technology 1939, H 1981 Fellowship in Chemical Engineering.

Notes and references

1 M. E. Cates and J. Tailleur, *Annual Review of Condensed Matter Physics*, 2015, **6**, 219–244.

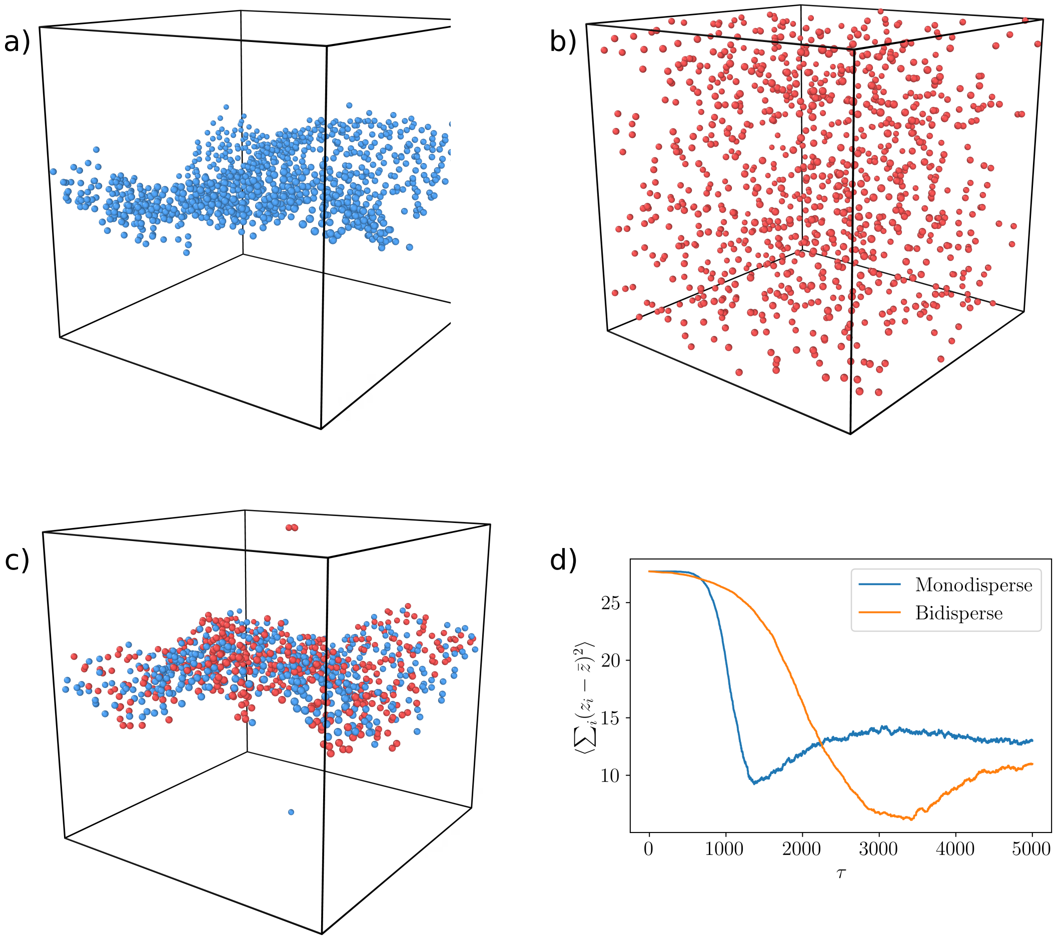

Fig. 12 Comparison of simulation results for monodisperse cases of $R=1$, $M=1$, a) $S=10$ (blue), b) $S=0.1$ (red), and c) $S_A=10$ (blue), $S_B=0.1$ (red). In all three cases a snapshot from τ_{final} is shown. d) Standard deviation of the z-position of all drops as a function of time, averaged over five runs with varying initial states, for the monodisperse case of $R=1$, $S=10$, and the bidisperse case of $R=1$, $S_A=10$, $S_B=0.1$.

2 J. Elgeti, R. G. Winkler and G. Gompper, *Reports on Progress in Physics*, 2015, **78**, 056601.

3 S. H. Klapp, *Current Opinion in Colloid & Interface Science*, 2016, **21**, 76–85.

4 T. Speck, *Soft Matter*, 2020, **16**, 2652–2663.

5 J. Zhang, R. Alert, J. Yan, N. S. Wingreen and S. Granick, *Nature Physics*, 2021, **17**, 961–967.

6 A. Al Harraq, M. Bello and B. Bharti, *Current Opinion in Colloid & Interface Science*, 2022, 101612.

7 K. J. Bishop, S. L. Biswal and B. Bharti, *Annual Review of Chemical and Biomolecular Engineering*, 2023, **14**, 1–30.

8 B. J. Nelson, I. K. Kaliakatsos and J. J. Abbott, *Annual Review of Biomedical Engineering*, 2010, **12**, 55–85.

9 D. Kagan, R. Laocharoensuk, M. Zimmerman, C. Clawson, S. Balasubramanian, D. Kang, D. Bishop, S. Sattayasamitsathit, L. Zhang and J. Wang, *Small*, 2010, **6**, 2741–2747.

10 A. Ghosh, W. Xu, N. Gupta and D. H. Gracias, *Nano Today*, 2020, **31**, 100836.

11 B. Jurado-Sánchez, S. Sattayasamitsathit, W. Gao, L. Santos, Y. Fedorak, V. V. Singh, J. Orozco, M. Galarnyk and J. Wang, *Small*, 2015, **11**, 499–506.

12 T. Ban, K. Tani, H. Nakata and Y. Okano, *Soft Matter*, 2014, **10**, 6316–6320.

13 Y. Zhang, K. Yan, F. Ji and L. Zhang, *Advanced Functional Materials*, 2018, **28**, 1806340.

14 M. Sun, W. Chen, X. Fan, C. Tian, L. Sun and H. Xie, *Applied Materials Today*, 2020, **20**, 100682.

15 Y. Fu, H. Yu, X. Zhang, P. Malgaretti, V. Kishore and W. Wang, *Micromachines*, 2022, **13**, 295.

16 W. Duan, W. Wang, S. Das, V. Yadav, T. E. Mallouk and A. Sen, *Annual Review of Analytical Chemistry*, 2015, **8**, 311–333.

17 J. L. Moran and J. D. Posner, *Annual Review of Fluid Mechanics*, 2017, **49**, 511–540.

18 S. Michelin, E. Lauga and D. Bartolo, *Physics of Fluids*, 2013, **25**, 061701.

19 W. F. Paxton, K. C. Kistler, C. C. Olmeda, A. Sen, S. K. St. Angelo, Y. Cao, T. E. Mallouk, P. E. Lammert and V. H. Crespi, *Journal of the American Chemical Society*, 2004, **126**, 13424–13431.

20 C. C. Maass, C. Krüger, S. Herminghaus and C. Bahr, *Annual Review of Condensed Matter Physics*, 2016, **7**, 171–193.

21 S. Michelin, *Annual Review of Fluid Mechanics*, 2023, **55**, 77–

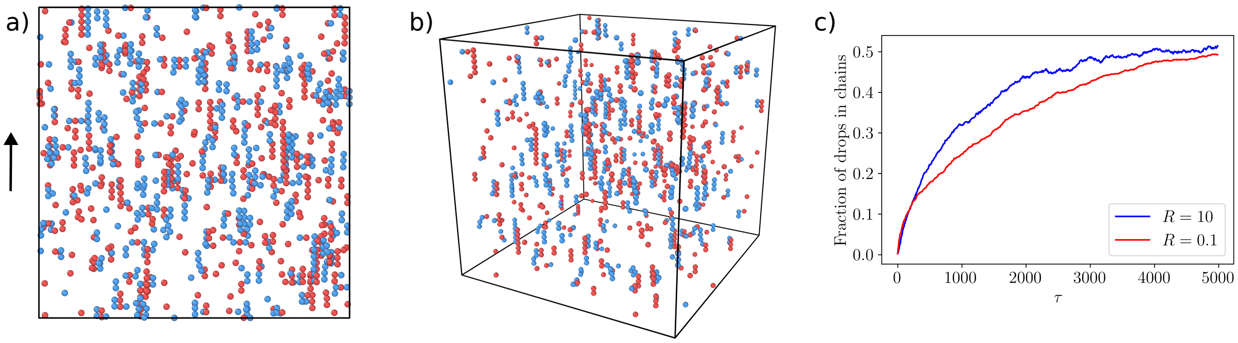

Fig. 13 Simulation results for $R_A = 10$ (blue), $R_2 = 0.1$ (red), $S = 1$, $M = 1$ in three dimensions. Field points in the vertical direction. a) Side view (xz plane) of τ_{final}. b) Three dimensional view of τ_{final} (Video S7, ESI†). c) Fraction of chained drops of each type (A versus B) as a function of time. A value of 1 on the vertical axis denotes that all drops of that type are in chains.

101.

22 S. Thutupalli, R. Seemann and S. Herminghaus, *New Journal of Physics*, 2011, **13**, 073021.

23 N. J. Suematsu, K. Saikusa, T. Nagata and S. Izumi, *Langmuir*, 2019, **35**, 11601–11607.

24 E. Lauga, *Annual Review of Fluid Mechanics*, 2016, **48**, 105–130.

25 I. S. Aranson, *Reports on Progress in Physics*, 2022, **85**, 076601.

26 R. V. Balaj and L. D. Zarzar, *Chemical Physics Reviews*, 2020, **1**, 011301.

27 C. C. Maass, *Journal of Fluid Mechanics*, 2023, **956**, F1.

28 G. Loget and A. Kuhn, *Nature Communications*, 2011, **2**, 535.

29 R. Dreyfus, J. Baudry, M. L. Roper, M. Fermigier, H. A. Stone and J. Bibette, *Nature*, 2005, **437**, 862–865.

30 H. Karani, G. E. Pradillo and P. M. Vlahovska, *Physical Review Letters*, 2019, **123**, 208002.

31 A. A. Harraq, B. D. Choudhury and B. Bharti, *Langmuir*, 2022, **38**, 3001–3016.

32 A. Boymelgreen, J. Schiffbauer, B. Khusid and G. Yossifon, *Current Opinion in Colloid & Interface Science*, 2022, **60**, 101603.

33 Y. Hong, M. Diaz, U. M. Córdova-Figueroa and A. Sen, *Advanced Functional Materials*, 2010, **20**, 1568–1576.

34 W. Wang, S. Li, L. Mair, S. Ahmed, T. J. Huang and T. E. Mallouk, *Angewandte Chemie International Edition*, 2014, **53**, 3201–3204.

35 G. Taylor, *Proceedings of the Royal Society of London. Series A. Mathematical and Physical Sciences*, 1966, **291**, 159–166.

36 J. R. Melcher and G. I. Taylor, *Annual Review of Fluid Mechanics*, 1969, **1**, 111–146.

37 D. A. Saville, *Annual Review of Fluid Mechanics*, 1997, **29**, 27–64.

38 P. M. Vlahovska, *Annual Review of Fluid Mechanics*, 2019, **51**, 305–330.

39 H. A. Pohl, *Journal of Applied Physics*, 1951, **22**, 869–871.

40 M. Washizu and T. Jones, *IEEE Transactions on Industry Applications*, 1996, **32**, 233–242.

41 J. C. Baygents, N. J. Rivette and H. A. Stone, *Journal of Fluid Mechanics*, 1998, **368**, 359–375.

42 M. Zabarankin, *Proceedings of the Royal Society A: Mathematical, Physical and Engineering Sciences*, 2020, **476**, 20190517.

43 T. B. Jones, *Electromechanics of particles*, Cambridge University Press, 2005.

44 H. Block and J. P. Kelly, *Journal of Physics D: Applied Physics*, 1988, **21**, 1661–1677.

45 M. Parthasarathy and D. J. Klingenberg, *Materials Science and Engineering R: Reports*, 1996, **17**, 57–103.

46 A. P. Hynninen and M. Dijkstra, *Physical Review Letters*, 2005, **94**, 8–11.

47 Z. M. Sherman, D. Ghosh and J. W. Swan, *Langmuir*, 2018, **34**, 7117–7134.

48 C. Sorgentone, J. I. Kach, A. S. Khair, L. M. Walker and P. M. Vlahovska, *Journal of Fluid Mechanics*, 2021, **914**, A24.

49 C. Sorgentone and P. M. Vlahovska, *Physical Review Fluids*, 2021, **6**, 053601.

50 J. I. Kach, L. M. Walker and A. S. Khair, *Physical Review Fluids*, 2022, **7**, 1–22.

51 C. Sorgentone and P. M. Vlahovska, *Journal of Fluid Mechanics*, 2022, **951**, R2.

52 A. V. Ivlev, J. Bartnick, M. Heinen, C. R. Du, V. Nosenko and H. Löwen, *Physical Review X*, 2015, **5**, 1–10.

53 M. Fruchart, R. Hanai, P. B. Littlewood and V. Vitelli, *Nature*, 2021, **592**, 363–369.

54 C. H. Meredith, P. G. Moerman, J. Groenewold, Y. J. Chiu, W. K. Kegel, A. van Blaaderen and L. D. Zarzar, *Nature Chemistry*, 2020, **12**, 1136–1142.

55 H. Sompolinsky and I. Kanter, *Physical Review Letters*, 1986, **57**, 2861–2864.

56 H. Hong and S. H. Strogatz, *Physical Review Letters*, 2011, **106**, 054102.

57 T. Ishikawa, M. P. Simmonds and T. J. Pedley, *Journal of Fluid Mechanics*, 2006, **568**, 119.

58 C. Pozrikidis, *Boundary Integral and Singularity Methods for Linearized Viscous Flow*, Cambridge University Press, Cambridge, 1992.

59 S. Kim and S. J. Karrila, *Microhydrodynamics: principles and*

selected applications, Dover Publications, Mineola, N.Y, 2005.

60 J. A. Anderson, J. Glaser and S. C. Glotzer, *Computational Materials Science*, 2020, **173**, 109363.

61 H. Hasimoto, *Journal of Fluid Mechanics*, 1959, **5**, 317–328.

62 J. Agudo-Canalejo and R. Golestanian, *Physical Review Letters*, 2019, **123**, 18101.

63 R. Soto and R. Golestanian, *Physical Review Letters*, 2014, **112**, 1–5.

64 D. Heyes and J. Melrose, *Journal of Non-Newtonian Fluid Mechanics*, 1993, **46**, 1–28.

65 D. R. Foss and J. F. Brady, *Journal of Rheology*, 2000, **44**, 629–651.

66 X. D. Pan and G. H. McKinley, *Journal of Colloid and Interface Science*, 1997, **195**, 101–113.

67 M. Grzelczak, J. Vermant, E. M. Furst and L. M. Liz-Marzán, *ACS Nano*, 2010, **4**, 3591–3605.

68 J. W. Swan, J. L. Bauer, Y. Liu and E. M. Furst, *Soft Matter*, 2014, **10**, 1102–1109.

69 V. Calandrini, E. Pellegrini, P. Calligari, K. Hinsen and G. Kneller, *École thématique de la Société Française de la Neutronique*, 2011, **12**, 201–232.

70 A. Spatafora-Salazar, D. M. Lobmeyer, L. H. Cunha, K. Joshi and S. L. Biswal, *Soft Matter*, 2021, **17**, 1120–1155.

71 F. Katzmeier, B. Altaner, J. List, U. Gerland and F. C. Simmel, *Physical Review Letters*, 2022, **128**, 058002.

72 J. S. Park and D. Saintillan, *Journal of Fluid Mechanics*, 2010, **662**, 66–90.

73 P. G. Moerman, H. W. Moyses, E. B. Van Der Wee, D. G. Grier, A. Van Blaaderen, W. K. Kegel, J. Groenewold and J. Brujic, *Physical Review E*, 2017, **96**, 032607.